ChemSusChem

Research Article
doi.org/10.1002/cssc.202501424

Chemistry Europe
European Chemical Societies Publishing

www.chemsuschem.org

Superior Performance and Catalytic Mechanism of an Icosahedral Quasicrystal Al-Cu-Fe in CO_2 Reduction to CO

Huixin Jin, Wenyang Zhang,* Haruka Yoshikawa, Asuka Ishikawa, Farid Labib, Boya Zhang, Jintao Zhou, Rongkai Kang, Jingyu Qin, Jianxin Zhang, Ya Xu,* and Ryuji Tamura*

Dissimilar to long-range periodic crystals, quasicrystals feature long-range aperiodic order and noncrystallographic rotational symmetry. These structural peculiarities and complexities endow it with unique properties and untold research values, together with significant challenges in decoding the structure–property relationship. Herein, the application of icosahedral quasicrystal (iQC) $Al_{63}Cu_{25}Fe_{12}$ as a high-performance catalyst is investigated for reducing CO_2 to CO, known as the reverse water–gas shift reaction, which is a key reaction for producing useful chemicals. Compared with the samples with similar compositions but different structures, it shows superior CO_2 conversion rate and CO selectivity. Combined with density functional theory calculations, the origin of the high catalytic activity of iQC $Al_{63}Cu_{25}Fe_{12}$ has been deciphered. It is found that for the approximant crystal of the quasicrystal, the reaction tends to occur near the icosahedral cluster. Compared to other control groups, it exhibits much lower reaction barriers during CO_2 reduction to CO. This demonstrates that the high catalytic performance of iQC $Al_{63}Cu_{25}Fe_{12}$ stems from its internally rich icosahedral cluster content. The research exemplifies the potential of quasicrystals in the field of catalysis and sheds light on the structure–property relationship of complex structures.

1. Introduction

Quasicrystals, characterized by their unique aperiodic order, exhibit a fascinating structural complexity that sets them apart from conventional crystalline materials. Unlike traditional crystals, which possess a repeating unit cell and exhibit long-range periodicity, quasicrystals showcase a well-defined, yet nonrepetitive arrangement of atoms, together with unusual rotational symmetries, such as fivefold or eightfold symmetry, which are not found in classical crystallography. The distinctive structural characteristics of quasicrystals provides unique properties and lucrative opportunities that are unobtainable elsewhere, leading to the development of multifarious applications, such as superconductivity,[1–3] magnetism,[4–7] hydrogen storage,[8] and corrosion and oxidation resistance.[9,10] However, past study on quasicrystals is rather inadequate. As for the application in catalysis, researchers have mostly focused on using quasicrystals as a substrate, with the catalytic centers being other materials attached to the surface, and the reactions involved are also quite limited. For example, Tsai and his coworkers[11–14] did a series of studies on the application of quasicrystals in catalysis and found that leachates obtained after etching the Al-Cu-Fe quasicrystal with an alkaline solution showed high catalytic activity and the excellent thermal stability in steam reforming of methanol. Research on using quasicrystals themselves as catalysts in various catalytic reactions is still far from sufficient.

The missing research pertains to the structural peculiarities and complexities of quasicrystals, especially the non-3D periodicity, has always been the formidable challenge that dissuades researchers from further investigation. To date, the most extensive and in-depth research aimed at uncovering structure–property relationships is limited to the low-index planes of simple structures.[15,16] The study on intricate systems, such as complex intermetallic compounds, whose unit cells are quite large, is sorely missing.[17] Quasicrystals, a special type of complex intermetallic compound featuring infinitely large unit cells, face the insurmountable challenge of deciphering their structure with theoretical approaches

H. Jin, J. Zhou, R. Tamura
Department of Materials Science and Technology
Tokyo University of Science
Tokyo 125-8585, Japan
E-mail: tamura@rs.tus.ac.jp

W. Zhang
Kagami Memorial Research Institute for Materials Science and Technology
Waseda University
2-8-26 Nishiwaseda, Shinjuku, Tokyo 169-0051, Japan
E-mail: w.iac23290@kurenai.waseda.jp

H. Yoshikawa, A. Ishikawa, F. Labib
Research Institute of Science and Technology
Tokyo University of Science
Tokyo 125-8585, Japan

B. Zhang, R. Kang, J. Qin, J. Zhang
School of Materials Science and Engineering
Shandong University
No. 17923, Jingshi Road, Jinan 250061, P. R. China

Y. Xu
Research Center for Energy and Environmental Materials
National Institute for Materials Science
3-13 Sakura, Tsukuba, Ibaraki 305-0003, Japan
E-mail: XU.Ya@nims.go.jp

Supporting information for this article is available on the WWW under https://doi.org/10.1002/cssc.202501424

and study the structure–property relationships and underlying mechanisms. Therefore, past research on the properties of quasicrystals has mostly focused on comparative analysis of experimental data, with little emphasis on theoretical analysis.

Here, we report the icosahedral quasicrystal (iQC) $Al_{63}Cu_{25}Fe_{12}$ as a high-performance thermal catalyst for the reverse water–gas shift (RWGS) reaction. The RWGS reaction can effectively use CO_2, a major contributor to the greenhouse effect and climate change, as a raw material to produce CO, which can then be converted into various value-added chemicals through subsequent Fischer–Tropsch synthesis.[18–22] In recent years, Cu- and Fe-containing catalysts have been widely investigated[20,23–30] as promising alternatives to noble metals (e.g., Pt) for the RWGS reaction due to their favorable activity-to-cost ratio. The iQC $Al_{63}Cu_{25}Fe_{12}$ in this work shows a CO_2 conversion rate of 43% at 500 °C and a weight hourly space velocity (WHSV) of 36 000 mL g^{-1} h^{-1}, much higher than those of other samples with similar compositions but different structures. The experimental characterizations demonstrate that the states and contents of different elements on the surfaces of iQC $Al_{63}Cu_{25}Fe_{12}$ and its control groups are generally similar, suggesting that the quasicrystal structure itself played a major role in the catalysis. Combining with density functional theory (DFT) calculations,[17,31–33] lower reaction barriers of iQC $Al_{63}Cu_{25}Fe_{12}$ toward RWGS are uncovered. The reactions are more likely to occur near the icosahedral clusters abundant within the iQC $Al_{63}Cu_{25}Fe_{12}$, thereby demonstrating that the quasicrystal structure itself contributes to the high catalytic activity of the reactions.

2. Results

2.1. Synthesis and Characterizations

The alloy of iQC $Al_{63}Cu_{25}Fe_{12}$ was prepared by mixing pure metals of Al, Cu, and Fe and melting it in an electric arc furnace under an argon atmosphere. After heat treatments, the pure phase ingot of iQC $Al_{63}Cu_{25}Fe_{12}$ was obtained. Under high-purity argon protection, the ingot was milled for different durations using a planetary ball mill (Experimental Section). In addition to the iQC $Al_{63}Cu_{25}Fe_{12}$ sample, two ternary complex intermetallic compounds (β-$Al_{55}Cu_{25}Fe_{20}$ and ω-$Al_{70}Cu_{20}Fe_{10}$) and two binary intermetallic compounds (Al_2Fe and θ-Al_2Cu) were selected as control groups. Compared with the quasicrystal, these control groups feature similar contents of active elements (Cu and Fe) and totally different crystal structures (Table 1, Supporting Information), providing the necessary basis to uncover the mechanism by which crystal structure influences the RWGS catalytic reaction.

X-ray diffraction (XRD) patterns were measured for iQC $Al_{63}Cu_{25}Fe_{12}$, β-$Al_{55}Cu_{25}Fe_{20}$, ω-$Al_{70}Cu_{20}Fe_{10}$, Al_2Fe, and θ-Al_2Cu before and after ball-milling to show the crystalline phases (**Figure 1**a–e). The XRD patterns of iQC $Al_{63}Cu_{25}Fe_{12}$, β-$Al_{55}Cu_{25}Fe_{20}$, ω-$Al_{70}Cu_{20}Fe_{10}$, Al_2Fe, and θ-Al_2Cu before ball-milling are well indexed to quasicrystal, cubic intermetallic (Pm-3 m), tetragonal intermetallic (P4/mnc), triclinic intermetallic (P-1), and tetragonal intermetallic (I4/mcm). The standard powder diffraction file cards are marked in the XRD patterns. The XRD patterns of all samples before ball milling exhibit sharp peaks with no obvious impurity peaks observed, indicating that these samples are single-phase with good crystallinity. It can be clearly observed that the peaks of all samples after ball-milling are broadened compared to those before ball-milling. It is the significant reduction in particle and grain sizes caused by the ball milling processes that results in the increase in the full width at half maximum of the diffraction peaks. In addition, an impurity phase different from the matrix can be observed on the XRD of θ-Al_2Cu after ball milling, corresponding to the cubic Al_4Cu_9 intermetallic phase (P43m). This indicates that the binary intermetallic compound has lower wear resistance and stability compared to ternary complex intermetallic compounds and quasicrystals, leading to phase separation during the ball-milling process.

Taking iQC $Al_{63}Cu_{25}Fe_{12}$ as an example, the scanning electron microscopy (SEM) images and particle size distribution histograms more intuitively reflect the changes in particle size with milling time (Figure 1, Supporting Information). As the ball-milling time increases, the particle size gradually decreases from tens of microns to submicron levels. However, when the ball milling time reaches 8 h, extending the milling time can hardly reduce the particle size any further, which is also evident from the graph showing particle size changes with ball-milling period (Figure 2, Supporting Information). For the other control groups, the same ball-milling process of 8 h was applied, and the resulting particle sizes are similar to that of iQC $Al_{63}Cu_{25}Fe_{12}$, all at the submicron level (Figure 3, Supporting Information). The nitrogen adsorption–desorption isotherm curves of iQC $Al_{63}Cu_{25}Fe_{12}$ after different time of ball-milling processes and the corresponding calculated specific surface areas in Figure 4, Supporting Information, indicate that with the increase in ball-milling time, the specific surface areas of iQC $Al_{63}Cu_{25}Fe_{12}$ also increases. However, after 8 h of ball milling, since further milling does not significantly reduce the particle size, the change in specific surface area becomes less noticeable. This trend can be observed more clearly in Figure 5, Supporting Information. Figure 6, Supporting Information, shows the nitrogen adsorption–desorption isotherm curves of β-$Al_{55}Cu_{25}Fe_{20}$, ω-$Al_{70}Cu_{20}Fe_{10}$, Al_2Fe, and θ-Al_2Cu before ball-milling for 8 h. After 8 h of ball-milling, iQC $Al_{63}Cu_{25}Fe_{12}$, β-$Al_{55}Cu_{25}Fe_{20}$, ω-$Al_{70}Cu_{20}Fe_{10}$, Al_2Fe, and θ-Al_2Cu exhibit similar specific surface areas (Figure 7, Supporting Information), and the catalyst performance variation induced by differences in specific surface area is accordingly excluded.

The morphology and crystal structures of all the samples were further characterized by high resolution transmission electron microscopy (HRTEM). Figure 1f–i presents the TEM results of iQC $Al_{63}Cu_{25}Fe_{12}$ before ball milling, where f–h show the selected area electron diffraction (SAED) patterns and corresponding HRTEM images at specific locations, respectively. The incident axes correspond to the quasicrystal's twofold, threefold, and fivefold rotational symmetry. These results further confirm the quasicrystal structure of the iQC $Al_{63}Cu_{25}Fe_{12}$. Figure 1i shows a locally magnified HRTEM image along the fivefold symmetry axis, revealing a richness of the icosahedral atomic structures within the quasicrystal. **Figure 2** shows the HRTEM images, SAED patterns, high-angle annular dark field (HAADF)

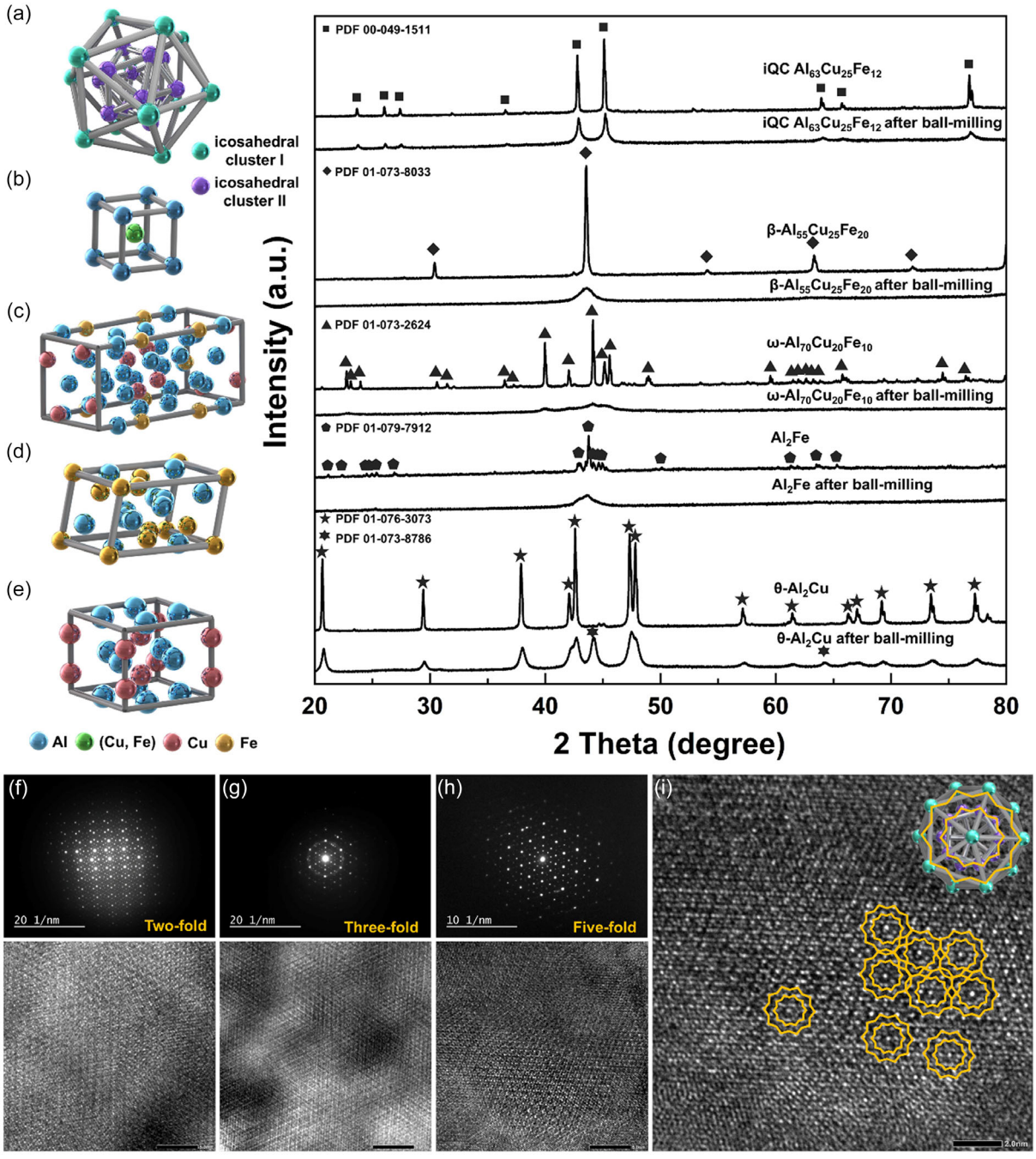

Figure 1. Phase structures of iQC $Al_{63}Cu_{25}Fe_{12}$ and its control groups (β-$Al_{55}Cu_{25}Fe_{20}$, ω-$Al_{70}Cu_{20}Fe_{10}$, Al_2Fe, and θ-Al_2Cu) before and after ball-milling. a–e) Atomic arrangements and XRD patterns of $Al_{63}Cu_{25}Fe_{12}$ and its control groups. The icosahedral clusters in (a) are used as a simplified representation of the quasicrystal structure. f–h) The SAED patterns and the HRTEM images of the corresponding areas of iQC $Al_{63}Cu_{25}Fe_{12}$ before ball-milling, with incidence axes along the twofold, threefold, and fivefold rotational symmetry. i) The locally enlarged HRTEM image of (h). Note that the inset in the top-right corner of (i) is a model of icosahedral clusters viewed from the fivefold axis. Based on this model, the icosahedral clusters in the image are marked with yellow lines.

images, and elemental energy disperse spectroscopy (EDS) mappings of iQC $Al_{63}Cu_{25}Fe_{12}$, β-$Al_{55}Cu_{25}Fe_{20}$, ω-$Al_{70}Cu_{20}Fe_{10}$, Al_2Fe, and θ-Al_2Cu after 8 h ball-milling. The consistency between the SAED patterns of iQC $Al_{63}Cu_{25}Fe_{12}$ after ball-milling and the diffraction pattern observed along the twofold symmetry axis of the quasicrystal before ball-milling verify that such post-processing procedure will not disrupt the quasicrystal structure (Figure 2 and 8, Supporting Information). Such structure consistency can also be found in the SAED patterns of iQC $Al_{63}Cu_{25}Fe_{12}$ along the threefold symmetry axis and that before ball milling (Figure 8, Supporting Information). For the powders of β-$Al_{55}Cu_{25}Fe_{20}$, ω-$Al_{70}Cu_{20}Fe_{10}$, Al_2Fe, and θ-Al_2Cu after ball milling, their SAED patterns were obtained along [111], [7-9-1], [3-4-1], and [313] axis, all corresponding to the crystal phases

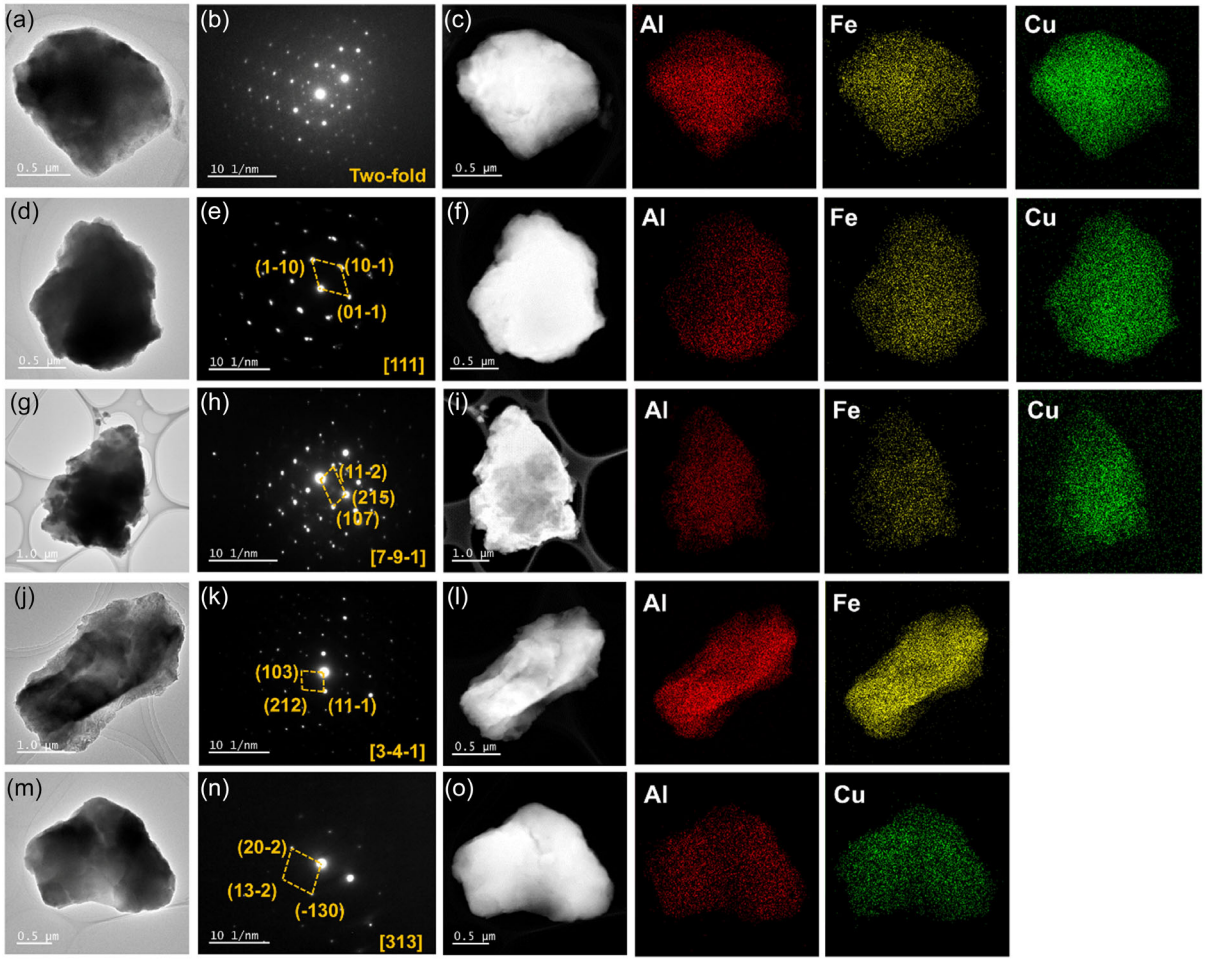

Figure 2. Microstructure and composition distributions of iQC $Al_{63}Cu_{25}Fe_{12}$ and its control groups after ball-milling. a,b) TEM image of iQC $Al_{63}Cu_{25}Fe_{12}$ after 8 h ball-milling and the SAED pattern observed along the twofold symmetry axis. c) HAADF images and corresponding EDS elemental mappings of iQC $Al_{63}Cu_{25}Fe_{12}$ after ball-milling. d,e) TEM image of β-$Al_{55}Cu_{25}Fe_{20}$ after ball-milling and the SAED pattern observed along the [111] zone axis. f) HAADF images and EDS mappings of β-$Al_{55}Cu_{25}Fe_{20}$ after ball-milling. g–o) TEM images, SAED patterns, HAADF images, and EDS mappings of other control groups (ω-$Al_{70}Cu_{20}Fe_{10}$, Al_2Fe, and θ-Al_2Cu) after ball-milling.

obtained from XRD, further confirming the crystal structures of these materials. The HAADF and EDS mappings of iQC $Al_{63}Cu_{25}Fe_{12}$, β-$Al_{55}Cu_{25}Fe_{20}$, ω-$Al_{70}Cu_{20}Fe_{10}$, Al_2Fe, and θ-Al_2Cu show uniform distributions of the constituent elements of the corresponding material without phase separation. The quantitative data of EDS in Table 2, Supporting Information, show the relative abundance of elements in all samples, which is generally consistent with the elemental composition of the corresponding materials.

X-ray photoelectron spectroscopy (XPS) spectra of iQC $Al_{63}Cu_{25}Fe_{12}$, β-$Al_{55}Cu_{25}Fe_{20}$, ω-$Al_{70}Cu_{20}Fe_{10}$, Al_2Fe, and θ-Al_2Cu were collected to reveal the element composition and further study the chemical state by conducting deconvolution (Figure 9, Supporting Information). The Al 2p spectrum of iQC $Al_{63}Cu_{25}Fe_{12}$ exhibits three peaks at 77.5, 74.6, and 72.2 eV, corresponding to hydroxide, Al_2O_3, and metal Al.[34] In Cu 2p spectrum shows only one peak at 932.4 eV, which is attributed to metal Cu. In Fe 2p spectrum, there are two main peaks located at 709.8 and 706.2 eV, which can be attributed to Fe_2O_3 and metal Fe.[35] Before and during the RWGS catalytic reaction, the catalysts were continuously protected by hydrogen, making the surface oxidation of the active elements Cu and Fe in the alloy powder negligible. However, during the XPS tests, the catalysts were exposed to air and inevitable oxidation of surface elements occurred, so the appearance of oxide peaks was quite reasonable.[36] The oxidation of the inactive (in terms of the RWGS reaction) element Al is inevitable when exposed to air.[34] The chemical states of the corresponding elements (particularly the active elements Cu and Fe) in the other control groups in Figure 9b–e, Supporting Information are essentially the same as those in iQC $Al_{63}Cu_{25}Fe_{12}$, which excludes the effects of this factor on catalytic performance.

2.2. Catalytic Performance in the RWGS Reaction

The thermal catalytic performance of iQC $Al_{63}Cu_{25}Fe_{12}$ and its control groups in RWGS reaction were evaluated at various temperatures. The activities in RWGS reaction are shown in **Figure 3**a. iQC $Al_{63}Cu_{25}Fe_{12}$ demonstrates the highest activity at all

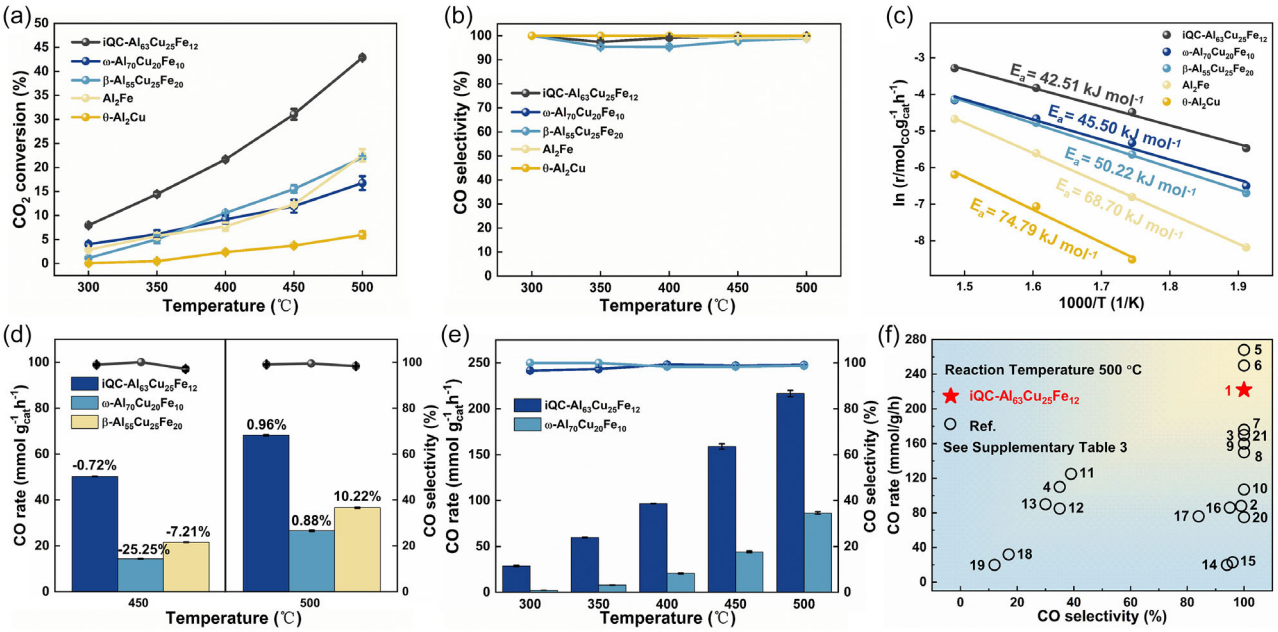

Figure 3. Evaluation of the catalytic performance of iQC $Al_{63}Cu_{25}Fe_{12}$ and its control groups in the RWGS reaction. a,b) CO_2 conversion and CO selectivity as a function of reaction temperature for different catalysts. c) Apparent activation energy values of iQC $Al_{63}Cu_{25}Fe_{12}$, β-$Al_{55}Cu_{25}Fe_{20}$, ω-$Al_{70}Cu_{20}Fe_{10}$, Al_2Fe, and θ-Al_2Cu catalysts. d) The performance of different catalysts obtained after completing the first round of RWGS testing, followed by cooling and conducting the second round of testing. The numbers above the bars represent the change in CO_2 conversion in the second round compared to the first round. e) The CO production rate and selectivity of iQC $Al_{63}Cu_{25}Fe_{12}$ and its control group obtained under the same feed ratio, space velocity, and other RWGS reaction conditions as used in Ref. [37]. f) Comparison of iQC $Al_{63}Cu_{25}Fe_{12}$ with previously reported non-noble catalysts and represented noble metal catalysts (numbers correspond to the line numbers in Table 3, Supporting Information).

temperatures, and at a reaction temperature of 500 °C, the CO_2 conversion of it reaches 43%. The differences in activity between iQC $Al_{63}Cu_{25}Fe_{12}$ and the other four samples are quite significant. Although the activities of the control groups showed some increase with rising temperatures, they remained at much lower levels. The CO_2 conversions of β-$Al_{55}Cu_{25}Fe_{20}$, ω-$Al_{70}Cu_{20}Fe_{10}$, Al_2Fe, and θ-Al_2Cu at 500 °C are 17%, 22%, 23%, and 6%, respectively. In addition, the CO selectivity of iQC $Al_{63}Cu_{25}Fe_{12}$ and its control groups were nearly 100% at all temperatures, with almost no CH_4 produced as a byproduct (Figure 3b). To further investigate the origin of the superior activity of iQC $Al_{63}Cu_{25}Fe_{12}$ in comparison to other control groups with similar compositions but different structures, the apparent activation energy E_a of each catalyst was analyzed from a kinetic perspective (Figure 3c). The E_a of iQC $Al_{63}Cu_{25}Fe_{12}$ is 42.51 kJ mol^{-1}, much lower than β-$Al_{55}Cu_{25}Fe_{20}$ (50.22 kJ mol^{-1}), ω-$Al_{70}Cu_{20}Fe_{10}$ (45.50 kJ mol^{-1}), Al_2Fe (68.70 kJ mol^{-1}), and θ-Al_2Cu (74.79 kJ mol^{-1}), indicating the much faster kinetics of iQC $Al_{63}Cu_{25}Fe_{12}$ catalyst in RWGS reaction.

To analyze the stability of catalysts with different structures, samples that were cooled to 100 °C after completing the first round of performance tests were subjected to a second round of RWGS performance tests. The CO_2 conversion and CO selectivity, as well as the corresponding rate of changes of iQC $Al_{63}Cu_{25}Fe_{12}$ and its control groups at 450 and 500 °C are shown in Figure 3d. It can be observed that, compared to the β and ω phases, the CO_2 conversion rate of the iQC $Al_{63}Cu_{25}Fe_{12}$ maintains at a relatively stable level at all temperatures, while the other two phases exhibit significant fluctuations. The activity differences between the quasicrystal and the β/ω phases are quite pronounced, with all catalysts demonstrating good selectivity for CO. These results indicate that the quasicrystal catalyst possesses superior stability compared to the β and ω phases. In addition, the stability of the quasicrystal was tested through five consecutive cycles and a long-term reaction at 500 °C, and the results indicated that the quasicrystal exhibited good stability (Figure 10, Supporting Information). To facilitate the comparison with literature data[37] on other catalysts used for the RWGS reaction, we employed the same feed ratios, space velocities, and other reaction conditions (Experimental Section) for the RWGS catalytic performance tests of both the iQC $Al_{63}Cu_{25}Fe_{12}$ and ω-$Al_{70}Cu_{20}Fe_{10}$ phases (Figure 3e). It can be observed that as the temperature rises, the difference in CO production rates between iQC $Al_{63}Cu_{25}Fe_{12}$ and its control groups becomes increasingly more obvious. At 400 °C, the reaction rate of iQC $Al_{63}Cu_{25}Fe_{12}$ reaches 96.8 mmol $gcat^{-1}$ h^{-1}, ≈4.7 times that of ω-$Al_{70}Cu_{20}Fe_{10}$ (20.6 mmol $gcat^{-1}$ h^{-1}). We also made a comparison between the CO production rate and selectivity of iQC $Al_{63}Cu_{25}Fe_{12}$ and various other reported non-noble or even noble metal catalysts (Figure 3f and Table 3, Supporting Information), where iQC $Al_{63}Cu_{25}Fe_{12}$ shows a certain superiority in both. Additionally, by varying the partial pressures of CO_2 and H_2, the reaction orders with respect to CO_2 and H_2 were determined to be 0.39 and 0.74 for iQC $Al_{63}Cu_{25}Fe_{12}$, and 0.50 and 0.49 for ω-$Al_{70}Cu_{20}Fe_{10}$, respectively (Figure 11, Supporting Information). This indicates that for iQC $Al_{63}Cu_{25}Fe_{12}$, the activation or participation step of hydrogen

is likely one of the rate-determining steps of the reaction. For ω-$Al_{70}Cu_{20}Fe_{10}$, the reaction rate is jointly controlled by the coadsorption of CO_2 and H_2 or their subsequent surface reaction step.

We also studied how the catalytic performance of iQC $Al_{63}Cu_{25}Fe_{12}$ changed with the ball-milling time and particle sizes (Figure 12, Supporting Information). Due to the ordered atomic occupancy and lack of translational symmetry in quasicrystals,

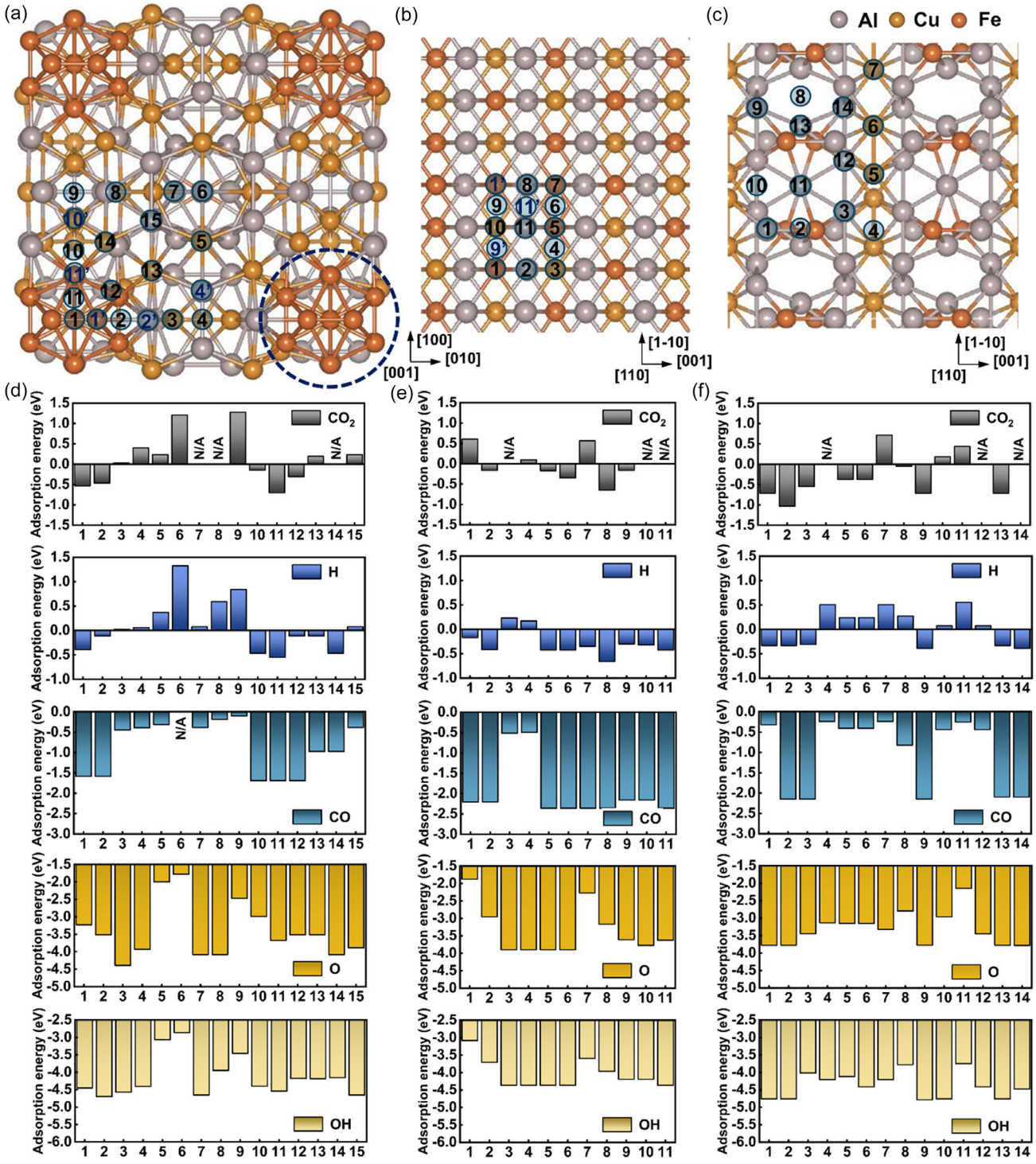

Figure 4. The adsorption characteristics of different adsorbates and intermediates related to the RWGS process at various adsorption sites of AC of the iQC-AlCuFe, β, and ω phases. a–c) The atomic structures and nonequivalent adsorption sites of the close-packed planes of the (a) AC, (b) β, and (c) ω phases. Noted that although the numbers n and n′ represent nonequivalent sites, after structural optimization, the final positions of the different adsorbates are identical. Therefore, only one site is counted in the analysis. The dashed circle highlights the icosahedral cluster within the AC structure. d–f) The adsorption energies of CO_2, H, CO, O, and OH at various adsorption sites of the (d) AC, (e) β phase, and (f) ω phase. N/A represents that the adsorbate does not adsorb at this site.

there are no well-defined slip systems, and dislocation motion requires the reconstruction of chemical bonds. When external stress is applied, the absence of effective plastic deformation mechanisms in these intermetallic compounds prevents stress relaxation. The inability to release stress through dislocation motion results in significantly higher brittleness compared to pure metals. As the ball-milling time increases from 0 to 10 h, the CO_2 conversion rises at different reaction temperatures (from 2% to 44% at 500 °C), with an increasing trend gradually slowing down, for the reduction of catalyst particle sizes with the increasing ball-milling time mitigates. This trend can be observed more clearly in Figure 12c, Supporting Information. Regardless of the ball-milling time, the CO selectivity of the iQC $Al_{63}Cu_{25}Fe_{12}$ catalyst consistently remained around 100%.

2.3. Reaction Mechanism of Different Catalysts

The above characterizations indicate the similar specific surface areas, chemical states, and contents of surface-active elements of these catalysts despite their different phase structures, so the difference in their phase structures is assumed to be the primary factor contributing to the significant differences in RWGS catalytic performances, for phase structures could exert major influence on the energy barriers during the conversion of reactants to products. To verify this hypothesis and further explore the intrinsic mechanisms by which different structures influence catalyst activity, we studied the potential mechanisms of the RWGS process on the surfaces of three catalysts: iQC, β, and ω, using first-principles calculations[31,32,38] based on DFT. Since quasicrystal does not have periodicity in three dimensions, we chose the simplest periodic approximant crystal (AC) of the iQC-AlCuFe, the 1/1 cubic approximant, as the model for calculations.[39] This model structure is the ideal structure obtained from the shear process of the iQC using the Katz, Gratias and Elser method.[39,40] It contains various cluster compositions, including the icosahedral clusters, and has been confirmed to be very similar in geometric and physical properties to iQC-AlCuFe.[41]

For the surfaces of the 1/1 AC, β, and ω phases, we selected the close-packed planes of each structure for analysis and calculated the adsorption energies of different adsorbates and intermediates related to the RWGS process at various adsorption sites, as shown in **Figure 4**a–c. The adsorption states of these adsorbates at each site after optimization are shown in Figure 13–27, Supporting Information. The adsorption energy of H at the most stable site of 1/1 AC is −0.55 eV, which is lower than that of β phase and higher than that of ω phase; the adsorption energy of CO_2 at the most stable site of 1/1 AC is −0.70 eV, which is

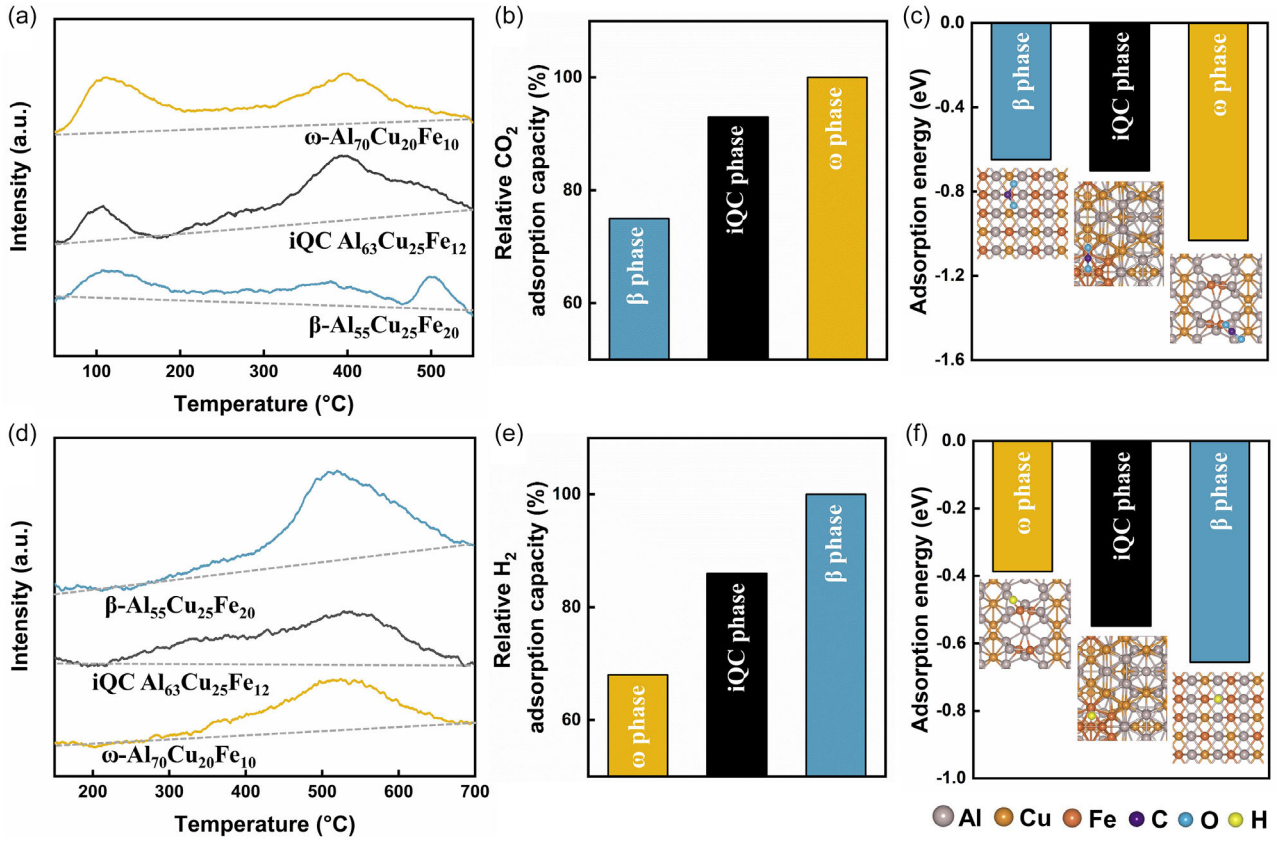

Figure 5. CO_2-TPD and H_2-TPD results of QC-AlCuFe, β, and ω phases, as well as the corresponding adsorption capacities, and the energy of the most stable adsorption sites of CO_2 and H on different structural surfaces. a–c) CO_2-TPD of QC-AlCuFe, β, and ω phases, as well as the adsorption energy of the most stable sites of CO_2 on surfaces of different phases. d–f) H_2-TPD of QC-AlCuFe, β, and ω phases, as well as the adsorption energy of the most stable sites of H on surfaces of different phases.

higher than that of β and lower than that of ω. In other words, compared to the β and ω catalysts featuring similar components but different structures, the quasicrystal exhibits moderate adsorption capabilities for each reactant, consistent with the Sabatier principle.[42] The CO_2 and H_2 temperature-programed desorption (TPD) results of the iQC-AlCuFe, β, and ω phases also experimentally support this point (**Figure 5**). The adsorption capacity of iQC-AlCuFe for CO_2 and H_2 lies between that of β and ω phases, consistent with the DFT calculation results. The CO adsorption capacity is also evaluated by CO-TPD tests (Figure 28, Supporting Information). The results reveals that the CO adsorption capacity of both the ω phase and iQC-AlCuFe is weaker than that of the β phase. Additionally, the comparison of the adsorption energy values at different sites on the 1/1 AC reveals that the stable adsorption sites for the reactants H and CO_2 are both located near the icosahedral clusters, indicating that the RWGS process is more likely to occur in proximity to these clusters.

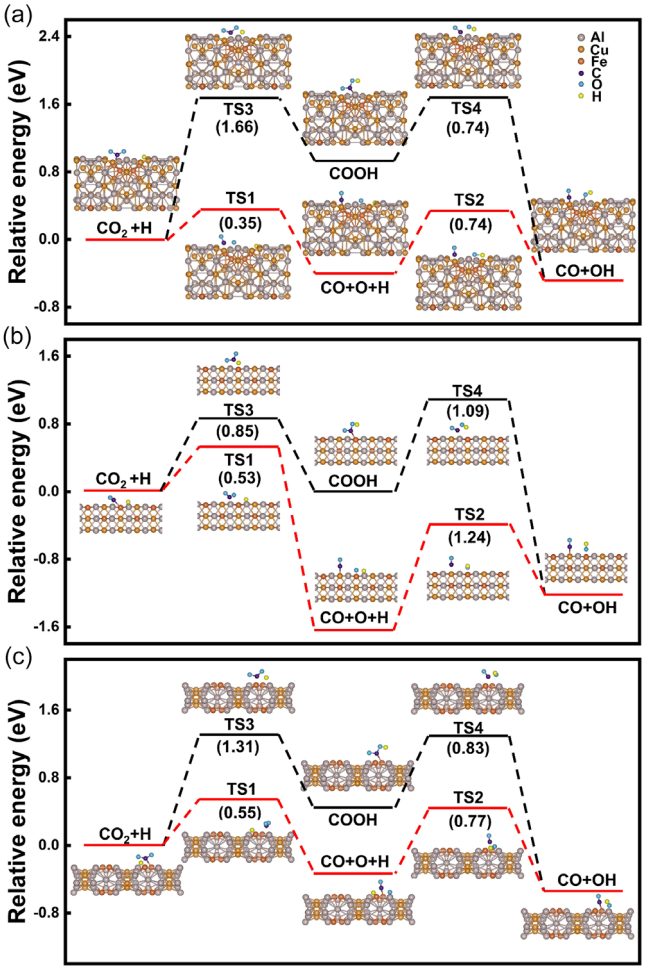

Figure 6. Reaction path and energy barriers for the RWGS reaction on different catalyst surfaces. a–c) Energy profiles for the direct dissociation and carboxylate mechanism on the (a) (001) AC, (b) (110) β, and (c) (110) ω surfaces. The values in parentheses indicate the energy barrier of the reaction. The red and black lines represent the direct dissociation pathway and the carboxylate pathway, respectively.

Numerous studies[20] have shown that catalysts containing element Fe and Cu typically proceed via two pathways during the RWGS reaction: one is the direct dissociation (redox) mechanism ($CO_2^* + H^* \rightarrow CO^* + O^* + H^*$, $CO^* + O^* + H^* \rightarrow CO^* + OH^*$), and the other is the carboxylate mechanism ($CO_2^* + H^* \rightarrow COOH^*$, $COOH^* \rightarrow CO^* + OH^*$). Thus, the energy barriers for both pathways on different catalyst surfaces were calculated, and the structures and energies of the various adsorption states and transition states are illustrated in **Figure 6**. It can be deduced that on the 1/1 AC and ω phase surfaces, the RWGS reaction prefers the direct dissociation mechanism, while on the β phase surface, it is more inclined to follow the carboxylate mechanism. By comparison, the energy barrier for the direct dissociation mechanism on the 1/1 AC surface is significantly lower than the barriers of β and ω phases for both of the two pathways. The barrier for the direct dissociation of CO_2 into CO and O on 1/1 AC surface is reduced to 0.35 eV, which facilitates the conversion from CO_2 to CO and is consistent with the experimentally measured significant increase in the CO formation rate. Therefore, on the 1/1 AC surface, the possibility of the RWGS reactions occurring near the icosahedral clusters is greater than at other locations, and the abundance of such structures (see Figure 1i) in iQC leads to lower energy barriers, which explain its superior CO formation rates and CO_2 conversion efficiency compared to the similarly composed β and ω phases. To verify whether the RWGS reaction on the quasicrystal surface tends to follow a direct dissociation mechanism, we conducted in situ time-resolved diffuse reflectance infrared fourier transform spectroscopy (DRIFTS) tests (**Figure 7**). It was observed that upon the introduction of CO_2, a significant amount of gaseous CO was formed, as indicated by two symmetrical peaks at ≈2140 cm^{-1} in the spectrum.[37] After switching to H_2, the band intensities for carboxylate (COOH, 1,666 cm^{-1}) and bidentate carbonate species (bi-CO_3^{2-}, 1545–1307 cm^{-1})[37] greatly increased. In contrast, the intensity of the gaseous CO band did not increase (as seen in the blue spectra after 1 and 5 min) but gradually decreased with the continued flow of H_2. These results suggest that during the RWGS reaction on the quasicrystal surface, CO_2 tends to dissociate directly into CO and O, which is consistent with the theoretical calculations

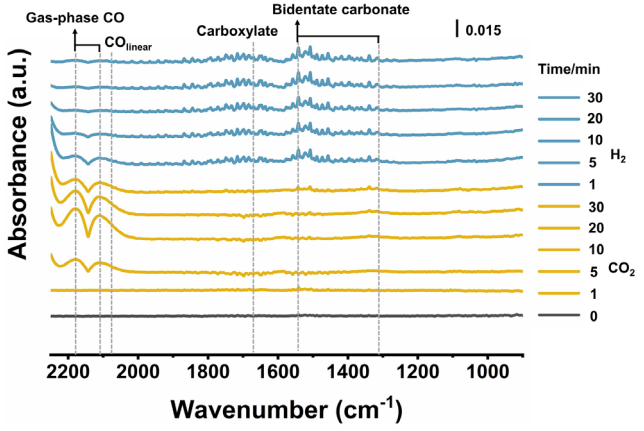

Figure 7. In situ time-resolved DRIFTS obtained over QC-AlCuFe when the feed gas was switched between CO_2 and H_2.

(Figure 6). Furthermore, the amount of linearly adsorbed CO (COlinear) was relatively weak, in agreement with the CO-TPD results (Figure 28, Supporting Information).

In this study, an iQC $Al_{63}Cu_{25}Fe_{12}$ is found to be a non-noble high-performance catalyst for the thermal catalytic RWGS reaction. By comparing the samples with similar compositions but different structures, the influence of catalyst surface area and elemental chemical states on catalytic performance are ruled out, highlighting the crucial role of the quasicrystal structure in this catalysis. Compared to these control groups, as well as other reported non-noble or even noble metal catalysts, the quasicrystal exhibits a higher CO production rate and selectivity. DFT calculations reveal lower reaction barriers of AC of iQC-AlCuFe during CO_2 reduction to CO compared with other samples. Paths with lower energy barriers are all near the icosahedral clusters, indicating that the high activity of iQC-AlCuFe for RWGS reaction is closely associated with the abundant icosahedral clusters in the quasicrystal. The discovery of structure–performance relationship of iQC also provides a reference for the intensive study of other complex structures.

3. Experimental Section

Preparation of iQC $Al_{63}Cu_{25}Fe_{12}$ Ingot and Its Control Groups

The Al-Cu-Fe alloys were prepared by melting a mixture of pure elements with purities of 99.9 wt% Al, 99.9 wt% Cu, and 99.9 wt% Fe in an electric arc furnace under an argon atmosphere. The phase structures and compositions of the alloys are shown in Table 1, Supporting Information. The cast ingots were sealed in quartz tubes filled with argon and annealed at 800, 700, 800, 1050, and 500 °C for 10, 24, 24, 72, and 72 h, respectively. They were then quenched in liquid nitrogen to obtain the pure phases of the iQC $Al_{63}Cu_{25}Fe_{12}$ and its control groups (β-$Al_{55}Cu_{25}Fe_{20}$, ω-$Al_{70}Cu_{20}Fe_{10}$, Al_2Fe, and θ-Al_2Cu).

Preparation of iQC $Al_{63}Cu_{25}Fe_{12}$ Powder and Its Control Groups

The heat-treated iQC $Al_{63}Cu_{25}Fe_{12}$ ingot and milling pot were placed in a glove box. Before crushing the ingot in a mortar, the container was vacuumed and filled with high-purity argon at least three times. The crushed 2 g ingot was placed in the milling jar along with 1 mL ethanol. Under the protection of high-purity argon, the ingot was milled for different durations (2, 4, 6, 8, and 10 h) using a planetary ball-milling machine (Pulverisette 6, Fritsch) to obtain alloy powders of varying sizes. During the milling process, the rotation speed was set to 400 r.p.m., and after every 10 min of milling, the rotation was paused for 2 min to release heat. After milling, the pot was opened in the glove box under high-purity argon protection, and the samples were collected for subsequent characterization and performance testing. The same method was used to mill the control groups for 8 h to collect alloy powders.

Materials Characterization

The phase structures of these materials before and after ball milling were characterized by XRD on a Rigaku SmartLab diffractometer equipped with a Cu Kα radiation ($\lambda = 0.15406$ nm). The particle sizes and surface morphologies of catalysts were observed with a ZEISS Gemini 560 SEM. Surface areas of alloy powders were measured with a Micromeritics ASAP 2020 instrument. These samples were first degassed at 150 °C for 3 h under vacuum. By using the N_2 adsorption–desorption isotherm at 77 K, surface areas were calculated by the Brunauer–Emmett–Teller method. The phase identification, microstructure observation, and composition analysis of these alloy powders were carried out using HAADF scanning transmission electron microscopy (JEOL JEM-2100F, with an acceleration voltage of 200 kV) and TEM-EDS (JEOL JED-2300, operating at 200 kV). XPS spectra were conducted on a JEOL JPS-9100.

Temperature-Programed Experiment

The CO_2, CO, or H_2 adsorption properties of the catalyst were evaluated by TPD (CO_2-TPD, CO-TPD, or H_2-TPD) on an AutoChem 2920 (Micromeritics Instrument) equipped with a thermal conductivity detector. The catalyst (100 mg) was pretreated at 430 °C for 1 h under a 10% H_2/Ar atmosphere, followed by purging with Ar for 30 min at 430 °C to remove the adsorbed H species. After cooling to 50 °C, high-purity CO_2, CO, or 10% H_2/Ar was preadsorbed for 30 min. Subsequently, the insert gas (30 mL min^{-1}, He for CO_2-TPD and CO-TPD, and Ar for H_2-TPD) was purged until the baseline stabilized. The TPD profile was then recorded as the temperature increased from 50 to 700 °C at a rate of 10 °C min^{-1}.

Catalytic Performance Evaluation

The catalytic performance of RWGS reaction was tested in a fixed-bed reactor (quartz; inner diameter, 8 mm). 100 mg catalyst was pretreated with H_2 (30 mL min^{-1}) at 703 K for 1h before the catalytic test. The composition of the reaction gas is 40vol% H_2/10vol% CO_2/50vol% N_2, and the total gas flow rate was set at 60 mL min^{-1}. The RWGS reaction test was conducted at the temperature range of 250–500 °C (measured at every 50 °C interval, with each temperature held for 30 min). The composition of the outlet product was studied by two on-line gas chromatographs equipped with thermal conductivity detectors (GL Science, GC323). H_2, N_2, CH_4, and CO were separated using a zeolite-packed column (Molecular Sieve 13X), while H_2O, CO_2, CH_3OH, and other byproducts were separated using a column packed with a porous polymer adsorbent (Porapak Q). The pipelines connecting the reactor and the gas chromatograph were heated to >393 K during the tests to make sure that all the products existed in gas form. The product mixture went through a cooling device to get rid of the liquid products, and the total flow rate of the remaining gaseous products was recorded using a flow meter (Mesa Laboratories, Defender530). The flow rate of each product was determined by analyzing the results of gas chromatographic and total flow rate measurements.

After completing the first round of performance testing, the samples were allowed to cool to 100 °C before conducting a second round of performance testing on the iQC $Al_{63}Cu_{25}Fe_{12}$ and its control groups to evaluate the stability of the quasicrystal and other catalysts. Additionally, to facilitate comparison with literature data[14] on other catalysts used in the RWGS reaction, the same feed ratios (72 vol% H_2/24 vol% CO_2/4 vol% N_2), space velocity (total gas flow rate was 100 mL min^{-1}, WHSV = 60 000 mL g^{-1} h^{-1}), atmospheric pressure and other reaction conditions were used for performance testing of the iQC $Al_{63}Cu_{25}Fe_{12}$ and its control groups. The CO formation rates of the iQC $Al_{63}Cu_{25}Fe_{12}$ are measured and compared with some reported catalysts, as detailed in Table 3, Supporting Information and Figure 3f.

The CO_2 conversion (C_{CO_2}), CO selectivity (S_{CO}), and CO production rates (R_{CO}) were calculated as follows

$$C_{CO_2} = \frac{F_{CO_2,in} - F_{CO_2,out}}{F_{CO_2,in}} \times 100\% \quad (1)$$

$$S_{CO} = \frac{F_{CO,out}}{F_{CO_2,in} - F_{CO_2,out}} \times 100\% \quad (2)$$

$$R_{CO} = \frac{F_{CO,out}}{\omega} \times 100\% \quad (3)$$

F_X is the flow rate of gas X (mmol h^{-1}), and ω is the mass of the catalyst.

The activation energy for the RWGS reaction was calculated based on performance data obtained during temperature-programed reactions in the range of 250–400 °C, with a CO_2 conversion of <15% (except iQC at 400 °C). The activation energy was estimated using the Arrhenius equation.[12]

Parameter Setting of DFT Calculations

All structural relaxation and energetic calculations were conducted via the DFT code—Vienna Ab Initio Simulation Package (VASP)[31] with periodic conditions and the plane-wave basis sets.[32] The interactions between electron ions were addressed using the method of projector-augmented wave theory.[43] Generalized gradient approximation method was used to analyze exchange-correlation energy.[44,45] The cut-off energy was set to 500 eV in all calculations. K-point sampling grids determined by Monkhorst–Pack method[46] were set to $3 \times 3 \times 3$, $11 \times 11 \times 11$, and $7 \times 7 \times 3$ for bulk iQC $Al_{63}Cu_{25}Fe_{12}$, β-$Al_{55}Cu_{25}Fe_{20}$, and ω-$Al_{70}Cu_{20}Fe_{10}$, respectively. Broyden Fletcher Goldfarb Shannon algorithm was utilized to relax the models and optimize the structures. For iQC $Al_{63}Cu_{25}Fe_{12}$, β-$Al_{55}Cu_{25}Fe_{20}$, and ω-$Al_{70}Cu_{20}Fe_{10}$ slabs, the k-points samplings were $2 \times 2 \times 1$, $3 \times 2 \times 1$, and $2 \times 3 \times 1$, respectively. 15 Å was used as the vacuum layer between periodically repeated slabs to avoid interactions among slabs. The energy changes in the structural optimization process and the maximum stress converge to 1.0×10^{-5} eV $atom^{-1}$ and 0.01 eV $Å^{-1}$, respectively. The climbing image nudged elastic band method is employed to obtain the transition state and energy barrier for different pathways. Three images between initial and final configurations are inserted and relaxed until the maximum residual force falls below 0.03 eV $Å^{-1}$.

The adsorption energies E_{ads} of different adsorbates and intermediates were calculated as follows

$$E_{ads} = E_{adsorbate/slab} - E_{slab} - E_{adsorbate} \quad (4)$$

where $E_{adsorbate/slab}$ is the total energy of the slab with the adsorbed species, E_{slab} is the total energy of the bare slab, and $E_{adsorbate}$ is the total energy of the adsorbate. According to this definition, a smaller value of E_{ads} corresponds to a stronger adsorption of a given species on the slab.

In situ *DRIFTS Experiment*

Prior to spectrum acquisition, the catalyst was reduced in a flow of 10% H_2/He (30 mL min^{-1}) at 703 K for 1 h. Subsequently, the catalyst was thoroughly purged with He for 2 h at the same temperature to remove any residual adsorbed H_2. Following this, the temperature was raised to 500 °C under a He flow. Upon reaching the target temperature, the catalyst was exposed to a flow of 10% CO_2/He (30 mL min^{-1}) for 30 min, and then switched to a flow of 10% H_2/He (30 mL min^{-1}).

Acknowledgements

This research was supported by the Japan Society for the Promotion of Science (JSPS Kakenhi grant no. 22F22348, JSPS Kakenhi grant no. 24F24036) and JST, CREST grant no. JPMJCR22O3, Japan.

Conflict of Interest

The authors declare no conflict of interest.

Data Availability Statement

The data that support the findings of this study are available from the corresponding author upon reasonable request.

Keywords: catalyst · CO_2 conversion · density functional theory · quasicrystal · reverse water–gas shift reaction

[1] Y. Tokumoto, K. Hamano, S. Nakagawa, Y. Kamimura, S. Suzuki, R. Tamura, K. Edagawa, *Nat. Commun.* **2024**, *15*, 1529.
[2] K. Kamiya, T. Takeuchi, N. Kabeya, N. Wada, T. Ishimasa, A. Ochiai, K. Deguchi, K. Imura, N. Sato, *Nat. Commun.* **2018**, *9*, 154.
[3] R. N. Araújo, E. C. Andrade, *Phys. Rev. B* **2019**, *100*, 014510.
[4] R. Takeuchi, F. Labib, T. Tsugawa, Y. Akai, A. Ishikawa, S. Suzuki, T. Fujii, R. Tamura, *Phys. Rev. Lett.* **2023**, *130*, 176701.
[5] R. Tamura, A. Ishikawa, S. Suzuki, T. Kotajima, Y. Tanaka, T. Seki, N. Shibata, T. Yamada, T. Fujii, C.-W. Wang, *J. Am. Chem. Soc.* **2021**, *143*, 19938.
[6] A. I. Goldman, T. Kong, A. Kreyssig, A. Jesche, M. Ramazanoglu, K. W. Dennis, S. L. Bud'ko, P. C. Canfield, *Nat. Mater.* **2013**, *12*, 714.
[7] R. Tamura, T. Abe, S. Yoshida, Y. Shimozaki, S. Suzuki, A. Ishikawa, F. Labib, M. Avdeev, K. Kinjo, K. Nawa, *Nat. Phys.* **2025**, 1.
[8] S. K. Verma, A. Bhatnagar, M. A. Shaz, T. P. Yadav, *Int. J. Hydrog. Energy* **2023**, *48*, 9762.
[9] S. Ryabtsev, V. Polonskyi, O. Sukhova, *Sci. Mater.* **2020**, *56*, 263.
[10] C. Zhou, F. Cai, H. Xu, S. Gong, *Mater. Sci. Eng. A* **2004**, *386*, 362.
[11] A. Tsai, M. Yoshimura, *Appl. Catal. A-Gen.* **2001**, *214*, 237.
[12] S. Kameoka, T. Tanabe, A. P. Tsai, *Catal. Today* **2004**, *93*, 23.
[13] T. Tanabe, S. Kameoka, A. P. Tsai, *Catal. Today* **2006**, *111*, 153.
[14] T. Tanabe, S. Kameoka, A. P. Tsai, *Appl. Catal. A-Gen.* **2010**, *384*, 241.
[15] J.r. Hafner, M. Krajci, *Acc. Chem. Res* **2014**, *47*, 3378.
[16] A. Jain, Y. Shin, K. A. Persson, *Nat. Rev. Mater.* **2016**, 1.
[17] H. X. Jin, J. X. Zhang, P. Li, Y. J. Zhang, W. Y. Zhang, J. Y. Qin, L. H. Wang, H. B. Long, W. Li, R. W. Shao, E. Ma, Z. Zhang, X. D. Han, *Nat. Commun.* **2022**, 13.
[18] Z. Xiao, C. Zhang, J. Gu, E. Yuan, G. Li, J.-J. Zou, D. Wang, *Chem. Eng. J.* **2025**, *507*, 160529.
[19] C. Zhang, Z. Xiao, X. Guo, X. Tan, J. Gu, J. Li, G. Li, J.-J. Zou, D. Wang, *Chem. Eng. J.* **2025**, 165414.
[20] E. Pahija, C. Panaritis, S. Gusarov, J. Shadbahr, F. Bensebaa, G. Patience, D. C. Boffito, *ACS Catal* **2022**, *12*, 6887.
[21] Z. Xiao, H. Zhang, X. Tan, F. Ye, Y. Zhang, J. Gu, J. Li, K. Sun, S. Zhang, J. J. Zou, *Adv. Energy Mater.* **2025**, *15*, 2500988.
[22] Z. Xiao, L. Zhang, X. Tan, K. Sun, J. Li, L. Pan, J. J. Zou, G. Li, D. Wang, *Adv. Funct. Mater.* **2025**, 2500339.
[23] H. Wang, M. S. Bootharaju, J. H. Kim, Y. Wang, K. Wang, M. Zhao, R. Zhang, J. Xu, T. Hyeon, X. Wang, *J. Am. Chem. Soc.* **2023**, *145*, 2264.
[24] K. de Kock, S. Raseale, W. Marquart, T. Verfaille, M. Claeys, N. Fischer, *ACS Catal.* **2025**, *15*, 5835.

[25] A. I. Rabee, H. Abed, T. H. Vuong, S. Bartling, L. Kraußer, H. Atia, N. Rockstroh, E. V. Kondratenko, A. Brückner, J. Rabeah, *ACS Catal.* **2024**, *14*, 10913.
[26] B. Lu, Z. Han, X. Zhi, L. Zhang, *Chem. Eng. J.* **2024**, *500*, 156844.
[27] A. M. Bahmanpour, F. Héroguel, M. Kılıç, C. J. Baranowski, P. Schouwink, U. Röthlisberger, J. S. Luterbacher, O. Kröcher, *Appl. Catal. B Environ.* **2020**, *266*, 118669.
[28] A. M. Bahmanpour, F. Héroguel, M. Kılıç, C. J. Baranowski, L. Artiglia, U. Röthlisberger, J. S. Luterbacher, O. Kröcher, *ACS Catal.* **2019**, *9*, 6243.
[29] M. Zhu, P. Tian, R. Kurtz, T. Lunkenbein, J. Xu, R. Schlögl, I. E. Wachs, Y. F. Han, *Angew. Chem.* **2019**, *131*, 9181.
[30] G. Kim, S. H. Ryu, H. Jeong, Y. Choi, S. Lee, J. H. Choi, H. Lee, *Angew. Chem.* **2023**, *135*, e202306017.
[31] G. Kresse, D. Joubert, *Phys. Rev. B* **1999**, *59*, 1758.
[32] G. Kresse, J. Furthmüller, *Phys. Rev. B* **1996**, *54*, 11169.
[33] H. Jin, J. Zhang, Y. Zhang, W. Zhang, S. Ma, S. Mao, Y. Du, Z. Wang, J. Qin, Q. Wang, *Mater. Charact.* **2022**, *183*, 111609.
[34] P. Barua, V. Srinivas, S. Dhabal, T. Ghosh, *J. Mater. Res.* **2002**, *17*, 1892.
[35] M. C. Biesinger, B. P. Payne, A. P. Grosvenor, L. W. M. Lau, A. R. Gerson, R. S. Smart, *Appl. Surf. Sci.* **2011**, *257*, 2717.
[36] C. Hansen, W. Zhou, E. Brack, Y. Wang, C. Wang, J. Paterson, J. Southouse, C. Copéret, *J. Am. Chem. Soc.* **2024**.
[37] H. Kang, L. Zhu, S. Li, S. Yu, Y. Niu, B. Zhang, W. Chu, X. Liu, S. Perathoner, G. Centi, *Nat. Catal.* **2023**, *6*, 1062.
[38] H. Jin, J. Zhang, W. Zhang, Y. Zhang, S. Mao, Y. Du, S. Ma, J. Qin, Q. Wang, *Intermetallics* **2023**, *152*, 107768.
[39] F. Puyraimond, M. Quiquandon, D. Gratias, M. Tillard, C. Belin, A. Quivy, Y. Calvayrac, *Found. Crystallogr.* **2002**, *58*, 391.
[40] H. Yamada, T. Takeuchi, U. Mizutani, N. Tanaka, *Mater. Res. Soc. Sympos. Proc.* **1999**, *553*, 117.
[41] A. Quivy, M. Quiquandon, Y. Calvayrac, F. Faudot, D. Gratias, C. Berger, R. Brand, V. Simonet, F. Hippert, *J. Phys. Condens. Matter.* **1996**, *8*, 4223.
[42] P. Sabatier, *La catalyse en chimie organique*, University of Michigan Library **1913**.
[43] P. E. Blöchl, *Phys. Rev. B* **1994**, *50*, 17953.
[44] J. P. Perdew, K. Burke, M. Ernzerhof, *Phys. Rev. Lett.* **1996**, *77*, 3865.
[45] N. Troullier, J. L. Martins, *Phys. Rev. B* **1991**, *43*, 1993.
[46] D. J. Chadi, *Phys. Rev. B* **1977**, *16*, 1746.

Manuscript received: July 5, 2025
Revised manuscript received: September 26, 2025
Version of record online: October 29, 2025